A flexible bio-inspired H$_2$-production photocatalyst

CrossMark

Junwei Fu[a], Bicheng Zhu[a], Wei You[a], Mietek Jaroniec[b], Jiaguo Yu[a,c,*]

[a] State Key Laboratory of Advanced Technology for Materials Synthesis and Processing, Wuhan University of Technology, Wuhan 430070, PR China
[b] Department of Chemistry and Biochemistry, Kent State University, Kent, OH 44242, USA
[c] Department of Physics, Faculty of Science, King Abdulaziz University, Jeddah 21589, Saudi Arabia

ARTICLE INFO

ABSTRACT

Photocatalytic hydrogen generation from water splitting offers a viable potential solution for utilizing solar energy. Here we report a feasible synthesis of flexible bio-inspired Zn$_{0.5}$Cd$_{0.5}$S@PAN (polyacrylonitrile) mat-shaped photocatalyst with leaf-like structure, which shows high photocatalytic H$_2$-production activity with a rate of 475 μmol h^{-1} per 50 mg of the photocatalyst and an apparent quantum efficiency of 27.4% at 420 nm. The hierarchically porous structure of the mat-shaped Zn$_{0.5}$Cd$_{0.5}$S@PAN greatly enhances the molecular diffusion/transfer kinetics, and enlarges the utilization efficiency of light through the multiple reflections and scattering effect. Moreover, a good dispersion of Zn$_{0.5}$Cd$_{0.5}$S nanoparticles (NPs) on the surface of PAN nanofibers prevents their aggregation. These features account for high H$_2$-production activity of Zn$_{0.5}$Cd$_{0.5}$S@PAN. Remarkably, the integrity and flexibility of Zn$_{0.5}$Cd$_{0.5}$S@PAN mat-shaped photocatalyst facilitate their separation and re-use after photocatalytic reaction. Hierarchically porous leaf-like mat-shaped photocatalysts with high photocatalytic activity and stability should also find potential applications in solar cells, catalysis, separation and purification processes.

1. Introduction

Since Fujishima and Honda reported photoelectrochemical water splitting in 1972 [1], the semiconductor-driven photocatalytic splitting of water has been considered as an ideal strategy to generate high-density and clean hydrogen energy from solar energy [2–8]. To date, however, the efficiency of water splitting on visible-light responsive photocatalysts is far from the requirement for practical applications [9–15]. Moreover, among known photocatalysts, the most efficient ones are usually nanopowders [16–25], the separation and recycle of which from reaction solution is another major technological obstacle for advancing their commercial applications. Accordingly, numerous attempts have been made toward development and large scale production of highly efficient and easily recyclable photocatalysts [26,27].

Recently, flexible energy-conversion systems have attracted a lot of attention due to their unique advantages, such as flexibility, shape integrity, light weight, repeatability and so on. They have been used in flexible lithium-ion batteries and flexible supercapacitors [28,29]. As reported, the flexible materials can withstand external forces, and keep the integrated shape after reaction. Thus, the use of flexible materials as photocatalysts could solve the recycling problem of nanopowder photocatalysts. Unfortunately, there are few flexible materials directly used as H$_2$-production photocatalysts.

As we know, the photosynthesis in nature (Fig. 1) mainly occurs on the chlorophylls immobilized on flexible skeletons of leaves, and the generated nutrients are transferred to the trunk through these skeletons. The flat and flexible shape of leaves can greatly increase the area available for light absorption and capture of reactants, and consequently, enhance the photosynthesis process. Moreover, the stomata in leaves are critical for diffusion and release of reactants and products (CO$_2$, H$_2$O and O$_2$). Inspired by nature, one could envision the immobilization of highly efficient nanoparticle photocatalysts on flexible substrates to construct leaf-like structured photocatalysts. However, weak interactions between substrate and photocatalyst nanoparticles can cause the stripping of photocatalysts, which seriously restrict their practical applications [30–33]. Polyacrylonitrile (PAN) nanofibers are very attractive polymers due to their flexibility, lightweight, chemical and light resistance. Though some semiconductor/PAN composite photocatalysts have been reported [34–36], the lack of intimate contact and uniform dispersion caused by the incompatibility between inorganic semiconductor and organic PAN led to the unsatisfied performance. In this study, we took advantage of the C≡N functional groups of PAN nanofibers and used them to capture metal cations from solutions via coordination-type interactions, which resulted in the uniform deposition of highly efficient photocatalyst nanoparticles on the surface of these nanofibers [37]. In addition, we utilized the propensity of PAN
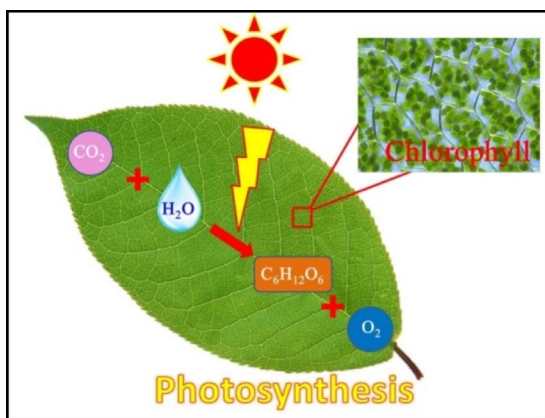
Fig. 1. The natural photosynthesis process occurring on leaves.

nanofibers to assembly into an integrated flexible mat through electrospinning. This mat has the same flat and flexible shape as a leaf, and features a hierarchically porous structure that can play a similar role as stomata in leaves. These special features make PAN mat a perfect flexible substrate candidate for constructing highly efficient leaf-like structured composite photocatalysts.

Herein, a flat and flexible PAN mat (PAN-Mat) is chosen as a substrate for immobilization of $Zn_xCd_{1-x}S$ solid solution photocatalyst nanoparticles. $Zn_{0.5}Cd_{0.5}S$ with sphalerite phase structure is the highly active solid solution nanosized photocatalyst for H_2-production as reported elsewhere [38,39]. The prepared leaf-like $Zn_{0.5}Cd_{0.5}S@PAN$ composite mat (ZCS@PAN-Mat) has intriguing properties due to the structural advantages of PAN mat and excellent photocatalytic H_2-production activity of $Zn_{0.5}Cd_{0.5}S$ NPs (ZCS-NP). Moreover, during the deposition of metal sulfides, PAN can be further sulfurized into sulfurized-PAN, which results in better affinity toward surface deposition of sulfides. This process favors uniform deposition of metal sulfides NPs ($Zn_{0.5}Cd_{0.5}S$) on the PAN mat. As a result, this integrated flexible ZCS@PAN-Mat shows high photocatalytic hydrogen evolution activity, even higher than that of the pure ZCS-NP. Cycle stability tests indicate that the flat and flexible composite mat exhibits good structure stability during photocatalytic hydrogen generation. The ZCS@PAN-Mat can be easily re-used without obvious loss of photocatalytic activity.

2. Experimental details

2.1. Synthesis of flexible PAN nanofibers mat (PAN-Mat)

PAN nanofiber mats were prepared via electrospinning method. Firstly, 1 g of PAN powder was completely dissolved in 10 mL of N, N'-dimethylformamide (DMF) and then the obtained transparent light-yellow solution was filled into a 20 mL syringe with a 0.6 mm inner-diameter metal needle. The details of electrospinning parameters, applied high voltage, feeding rate of the solution and distance between the needle and collection plate, were set at 15 kV, 0.5 mL/h and 15 cm, respectively. After electrospinning for approximately 10 h, the white PAN flexible mat was peeled off from the collection plate and dried at 80 °C.

2.2. Synthesis of $Zn_{0.5}Cd_{0.5}S@PAN$ flexible mat (ZCS@PAN-Mat)

In a typical synthesis of ZCS@PAN-Mat, 0.5 mmol of zinc acetate dihydrate, 0.5 mmol of cadmium acetate dihydrate and 2 mmol of thiourea were dissolved into 40 mL of ethanol to form a mixture solution, and then, a piece of integrated PAN-Mat (50 mg) was dipped into the above solution. After sonication for 10 min, the solution with PAN-Mat was transferred into a Teflon-lined stainless-steel autoclave with a total volume of 50 mL and kept at 120 °C for 12 h. After cooling down,

the resulting yellow ZCS@PAN-Mat was washed with water and ethanol thoroughly, and then dried in oven at 80 °C. For the purpose of comparison, pure $Zn_{0.5}Cd_{0.5}S$ nanoparticles (ZCS-NP), CdS nanoparticles (CS-NP) and ZnS nanoparticles (ZS-NP) were also prepared by the same method just without PAN-Mat. The CdS@PAN flexible mat (CS@PAN-Mat) and ZnS@PAN flexible mat (ZS@PAN-Mat) were prepared using 1 mmol of cadmium acetate dihydrate or 1 mmol of zinc acetate dihydrate to replace 0.5 mmol of zinc acetate dihydrate and 0.5 mmol of cadmium acetate dihydrate. The SPAN-Mat was prepared without the addition of Zn and Cd precursors, the other steps were the same as that in the case of ZCS@PAN-Mat.

2.3. Photocatalytic hydrogen evolution experiment

The photocatalytic hydrogen evolution experiments were performed in a 200 mL cylindrical Pyrex flask with three openings sealed by silicone rubber septa. A 350 W Xe lamp was used as light source to trigger the photocatalytic reaction. A filter was positioned between the light source and reactor to cut off UV light (≤ 420 nm). The distance between light source and reactor was set as 15 cm. In a typical photocatalytic reaction, a piece of prepared ZCS@PAN-Mat (50 mg) was soaked in 80 mL of mixture solution containing Na_2S (0.35 M) and Na_2SO_3 (0.25 M). Bubbled with N_2 for 20 min, the flask was sealed and irradiated using visible light for several hours. The generated H_2 gas was analyzed by a Shimadzu GC-14C gas chromatograph with TCD detector for every hour. The apparent quantum efficiency (QE) of photocatalytic reaction was measured using the same reaction conditions except that the light source was four LEDs with 420 nm wavelength. The distance between these LEDs and reactor was set as 1 cm. At this distance, the light intensity of each LED was measured to be 6.0 mW cm^{-2}. The irradiation area on the reactor for each LED was about 1 cm^2. The QE was calculated by using the following Eq. (1):

$$QE[\%] = \frac{number\,of\,reacted\ electrons}{number\,of\,incident\,photons}*100\%$$
$$= \frac{number\ of\,evolved\,H_2\ molecules\ *\ 2}{number\ of\,incident\,photons}*100\%$$

(1)

2.4. Electrochemical impedance spectra (EIS) measurements

EIS measurements were performed on an electrochemical analyzer (CHI660C Instruments) equipped with a standard three-electrode system. A Pt wire acted as the counter electrode, the Ag/AgCl (saturated KCl) as the reference electrode, and the FTO glass coated by the sample as the working electrode. The sample area on the FTO glass was about 1.5 cm^2. A UV-LED (3 W, 365 nm, Shenzhen LAMPLIC Science Co. Ltd., China) was used as light source and 0.5 M Na_2SO_4 was used as the electrolyte. The electrochemical impedance spectra (EIS) were recorded over a frequency range of $1–10^5$ Hz with an amplitude of 5 mV at 0.5 V.

2.5. Characterization

The X-ray diffraction (XRD) patterns were collected on a Rigaku D/Max-RB X-ray diffractometer (Japan) with Cu $K\alpha$ radiation at a scan rate (2θ) of 0.05° s^{-1}. A field emission scanning electron microscope (FESEM, JEOL 7500F, Japan) and a high-resolution transmission electron microscopy (TEM, JEOL 2100, Japan) were employed for the morphology and microstructure observations. Nitrogen adsorption and desorption isotherms were measured using a gas adsorption analyzer (Micromeritics ASAP 2020, USA). The pore size distribution curves were obtained by the Barret–Joyner–Halender (BJH) method using adsorption branches of adsorption-desorption isotherms. The light absorbance performance of the samples was investigated on a Shimadzu UV-2600 UV–vis spectrophotometer (Japan). The chemical composition of the samples and the chemical states of elements were characterized

by X-ray photoelectron spectroscopy (XPS, VG ESCALAB 210) with Mg $K\alpha$ radiation. The actual amounts of Zn and Cd in the samples were measured by inductively coupled plasma atomic emission spectrometry (ICP-AES, Optima 4300 DV, Perkin Elmer). The photoluminescence emission lifetimes of the samples were obtained by a time-resolved transient photoluminescence (PL) spectroscopy (FLS920 Edinburgh Instrument, UK).

2.6. Computational details

Density functional theory (DFT) calculations were carried out using the CASTEP Package. The Perdew−Burke−Ernzerhof (PBE) of the generalized gradient approximation (GGA) was used as the exchange-correlation function. An energy cutoff of 400 eV and the Monkhorst–Pack k-point mesh of $4 \times 4 \times 1$ were used to perform geometry optimizations. The energy and force convergence criterions were set as 1.0×10^{-5} eV/atom and 0.03 eV/Å, respectively.

3. Results and discussion

3.1. Morphology and microstructure

Field emission scanning electron microscopy (FESEM) and transmission electron microscope (TEM) were used to investigate the morphology and microstructure of the samples. The corresponding FESEM and TEM images are shown in Fig. 2. The macroscopic photographs of the as-prepared PAN-Mat and ZCS@PAN-Mat are shown in the left and right panels of Fig. 2a, respectively. These pictures show two integrated nonwoven-like mats having a size of approximately 3×3 cm and uniform color: PAN-Mat is gray-white, while ZCS@PAN-Mat is yellow. The evenly yellow color indicates a uniform distribution of $Zn_{0.5}Cd_{0.5}S$ NPs in ZCS@PAN-Mat. Fig. 2b shows a bending experiment performed on these two mats. Namely, these photographs show high flexibility of PAN-Mat and ZCS@PAN-Mat. Moreover, a movie (see Movie S1 in the Supporting Information) further shows that ZCS@PAN-Mat can be folded randomly without any destruction of the integrated structure. This advantage implies that it should exhibit sufficient strength during photocatalytic reactions and can be easily separated and re-used from photocatalytic reaction solution. The FESEM image of PAN-Mat (Fig. 3) shows uniform PAN nanofibers with diameters ranging from ~400 nm to ~600 nm. Another high magnification image indicates that the surface of PAN nanofibers is smooth without any secondary structure (Fig. 3b), which is not the case for ZCS@PAN-Mat. As shown in Fig. 2c, the surface of nanofibers in ZCS@PAN-Mat is highly rough. A high-magnification FESEM image (Fig. 2d) clearly shows that the surface of nanofibers in ZCS@PAN-Mat is covered by NPs. As a result, the diameters of nanofibers (about 1 μm) are much greater than those of pure PAN nanofibers (400–600 nm). It can be concluded that the $Zn_{0.5}Cd_{0.5}S$@PAN core-shell nanofibers were formed by immobilizing $Zn_{0.5}Cd_{0.5}S$ NPs onto the surface of PAN nanofibers. The contrast of edge and middle section of the composite nanofiber in TEM image (Fig. 2e) further confirms the formation of a core-shell heterostructure with an imitate contact between $Zn_{0.5}Cd_{0.5}S$ and PAN. One-dimensional (1D) core–shell nanostructures are distinctly advantageous because they assure a rapid electron transport along their axial direction [40,41]. Also, the imitate contact between $Zn_{0.5}Cd_{0.5}S$ and PAN indicates strong interactions between $Zn_{0.5}Cd_{0.5}S$ and the surface of PAN, which assures the structure stability of the resulting composite photocatalyst during photocatalytic reactions. In addition, the high-resolution TEM image (Fig. 2f) shows that the surface of PAN nanofibers is covered with NPs. This is highly consistent with the FESEM image in Fig. 2d. The visible lattice fringes with interplanar distance of 0.31 nm can be observed in the high-resolution TEM images of NPs on the surface of ZCS@PAN-Mat (Fig. 3c), which are ascribed to the (111) facets of $Zn_{0.5}Cd_{0.5}S$. In order to investigate the dispersion uniformity of $Zn_{0.5}Cd_{0.5}S$, the EDS mapping analysis of nanofibers in ZCS@PAN-Mat

is shown in Fig. 2g, indicating that Zn, Cd and S elements are evenly distributed on the surface of nanofibers. The uniform distribution of $Zn_{0.5}Cd_{0.5}S$ NPs results in evenly yellow color of ZCS@PAN-Mat.

3.2. Phase structure and surface properties

The XRD analysis was used to investigate the crystal structure of the prepared samples; the corresponding patterns are shown in Fig. 4a. The diffraction pattern of pure $Zn_{0.5}Cd_{0.5}S$ NPs (ZCS-NP) is characteristic for $Zn_{0.5}Cd_{0.5}S$ solid solution having sphalerite phase structure [38,39,42]. The main peak located at 26.5° can be assigned to (111) facets of $Zn_{0.5}Cd_{0.5}S$. Both the CdS@PAN composite mat (CS@PAN-Mat) and ZnS@PAN composite mat (ZS@PAN-Mat) exhibit sphalerite phase structure of CdS (JCPDS card no. 65-2887) and ZnS (JCPDS card no. 05-0566), respectively [43–45]. While, another control sample, PAN-Mat, just shows two characteristic peaks located at 16.8° and 21.5°, corresponding to the orthorhombic PAN [46]. In the case of ZCS@PAN-Mat, the XRD pattern can be seen as a combination of XRD patterns of PAN-Mat and ZCS-NP. These results demonstrate a good integration of these two components in ZCS@PAN-Mat, and the same crystal structures of $Zn_{0.5}Cd_{0.5}S$ solid solution in ZCS-NP and ZCS@PAN-Mat.

The specific surface area and porosity of the samples were investigated on the basis of N_2 adsorption-desorption data. The corresponding adsorption-desorption isotherms and pore size distribution curves are shown in Fig. 4b. In the case of PAN-Mat, a typical IV-type isotherm with H3-type hysteresis loop (relative pressure $P/P_0 = 0.7$–1.0) is observed, indicating the presence of slit-shaped mesopores [47], which are formed by accumulation of PAN nanofibers in the mat. Also type IV isotherm was measured for ZCS-NP, although in this case adsorption is enhanced at low pressures, which can be an indication of some microporosity [47] due to the aggregation of small primary $Zn_{0.5}Cd_{0.5}S$ NPs. The visible narrow hysteresis loop suggests the presence of mesopores, which can be formed by aggregation of secondary $Zn_{0.5}Cd_{0.5}S$ NPs consisted of primary $Zn_{0.5}Cd_{0.5}S$ NPs. For the ZCS@PAN-Mat, the isotherm is also type IV with possible small microporosity due to some enhancement of adsorption at low pressures. Due to the presence of micropores, ZCS-NP exhibits high specific surface area (125 m^2/g), much larger than that of PAN-Mat (9 m^2/g). The specific surface area of ZCS@PAN-Mat (51 m^2/g) is between those of PAN-Mat and ZCS-NP. The pore size distributions shown in the inset of Fig. 4b further confirm the presence of pores. The slit-shaped pores in PAN-Mat are large mesopores (~20 nm) and macropores (above 50 nm). The pore size distribution curve of ZCS-NP exhibits a high value at 2 nm. Though there is no data recorded when the pore is less than 2 nm (due to the experimental limit), the high adsorption at low relative pressure and a high value of pore size distribution curve at 2 nm both indicate that ZCS-NP should contain amount of micropores (below 2 nm). In summary, the ZCS-NP powder contains micropores and some mesopores (5–30 nm). The ZCS@PAN-Mat has three types of pores: microspores (< 2 nm), mesopores (2–50 nm) and slit-shaped macropores (50–100 nm), indicating hierarchically porous structure of ZCS@PAN-Mat. Such hierarchically porous structure is extremely beneficial for the diffusion of reactants and products due to the presence of efficient transport pathways. Moreover, hierarchical porosity can create longer light traveling path due to the multiple light reflection and scattering within the pore channels, resulting in better light utilization efficiency.

The light absorbance performance of the samples is closely related to the photocatalytic efficiency. To further discuss this issue, the UV–vis diffuse reflection spectra of ZCS-NP and ZCS@PAN-Mat are shown in Fig. 4c. The spectrum of ZCS@PAN-Mat shows a trailing phenomenon between 500 nm and 600 nm, which can be ascribed to the multiple light reflection and scattering effect of its hierarchically porous structure. Similarly, the spectrum of ZS@PAN-Mat exhibits more obvious trailing phenomenon between 600 nm and 350 nm due to the hierarchically porous structure (600–500 nm) and partially sulfurized PAN
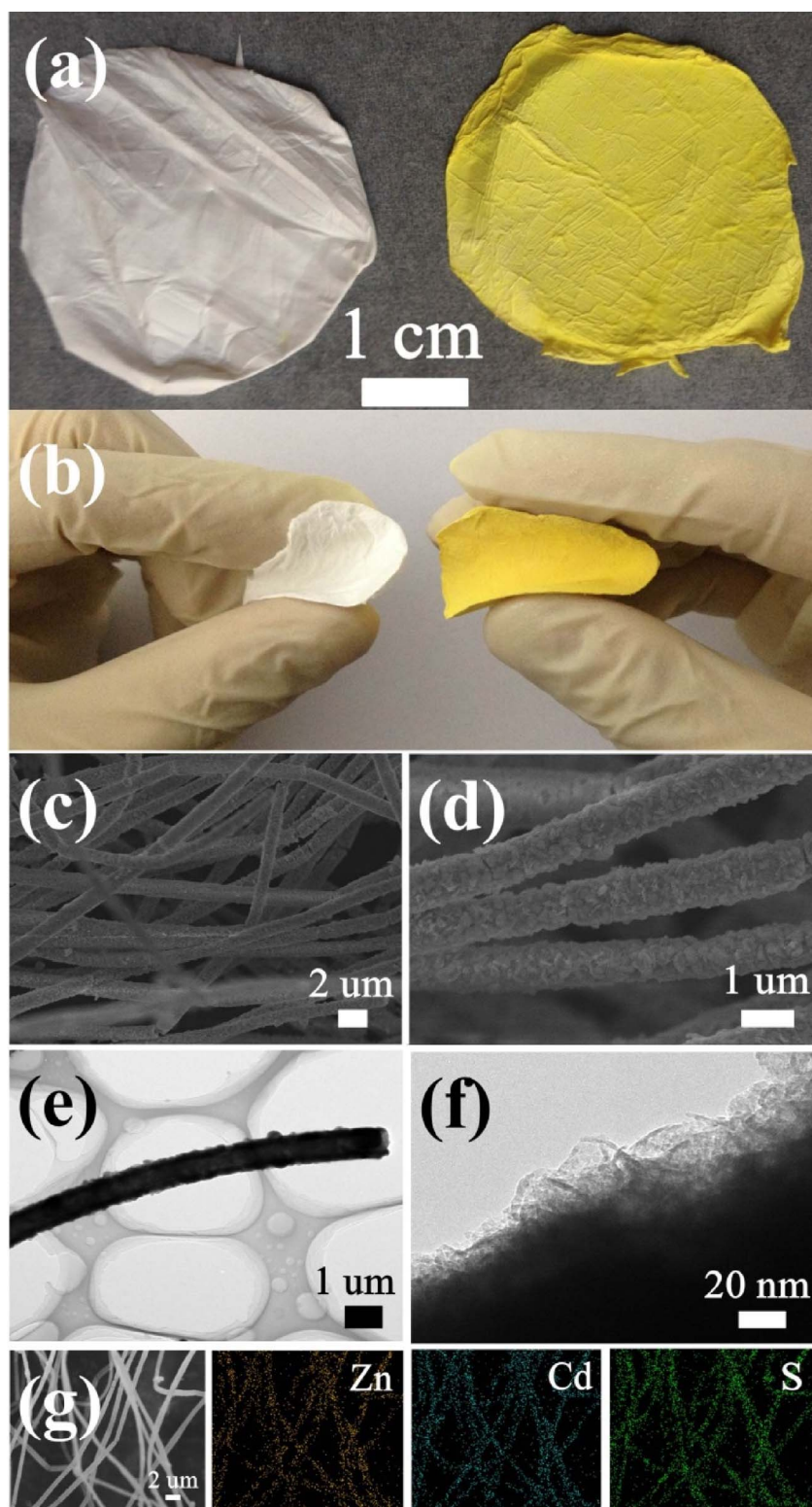
Fig. 2. (a and b) Macroscopic photographs of the PAN-Mat (left) and ZCS@PAN-Mat (right). (c, and d) FESEM, (e) TEM and (f) HRTEM images of ZCS@PAN-Mat. (g) FESEM and EDS mapping images of several $Zn_{0.5}Cd_{0.5}S@PAN$ core-shell nanofibers in ZCS@PAN-Mat.

nanofibers (500–350 nm). The trailing phenomenon of CS@PAN-Mat is covered by the intrinsic absorption of CdS. In order to investigate the sulfurization of PAN nanofibers, the spectrum of the sulfurized-PAN nanofibers mat (SPAN-Mat) is also provided. Clearly, it shows an enhanced absorption than that of PAN-Mat below 550 nm. This is important evidence, indicating that PAN was partially sulfurized during solvothermal process. In Fig. 4c, both ZCS-NP and ZCS@PAN-Mat show significant increase in the absorption at wavelengths shorter than

500 nm. It can be assigned to the intrinsic band-gap absorption of the $Zn_{0.5}Cd_{0.5}S$. According to the Kubelka-Munk function, the band-gap energies of ZCS-NP and ZCS@PAN-Mat were estimated to be 2.48 and 2.52 eV, respectively. On the basis of previous reports, the band gap energy would change with the variation of the Zn/Cd ratio in the $Zn_xCd_{1-x}S$ solid solution [38,48,49]. The bandgap of ZCS affected by PAN can be ignored due to the non-light-response of PAN. Herein, a small difference in the band-gap energy means the Zn/Cd ratios in ZCS-
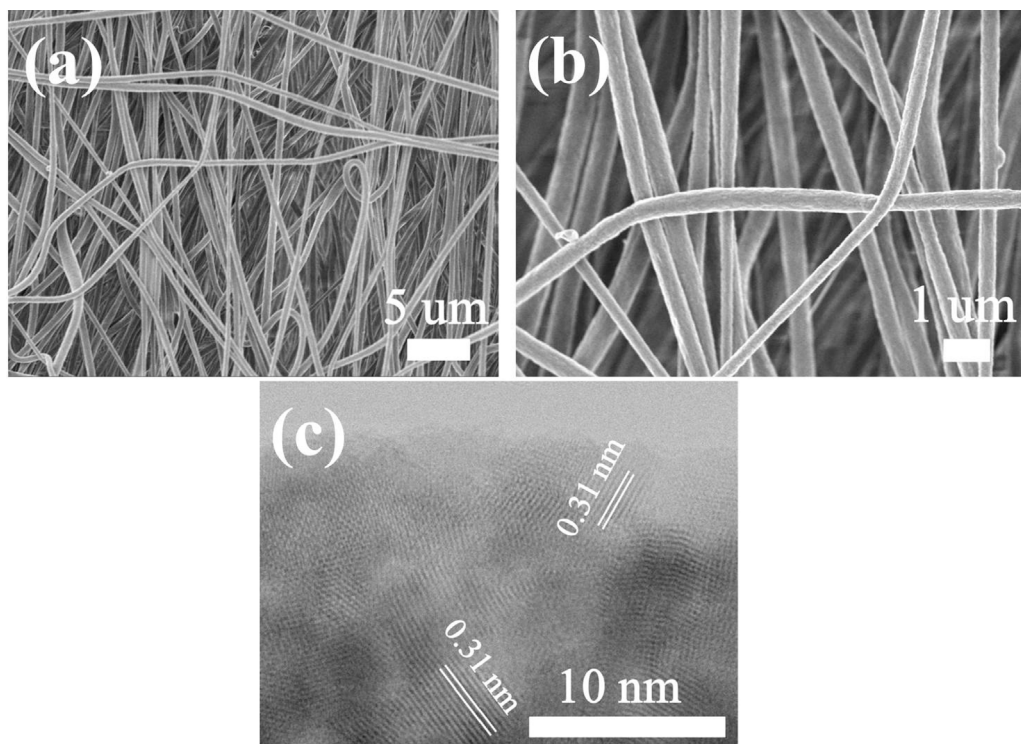
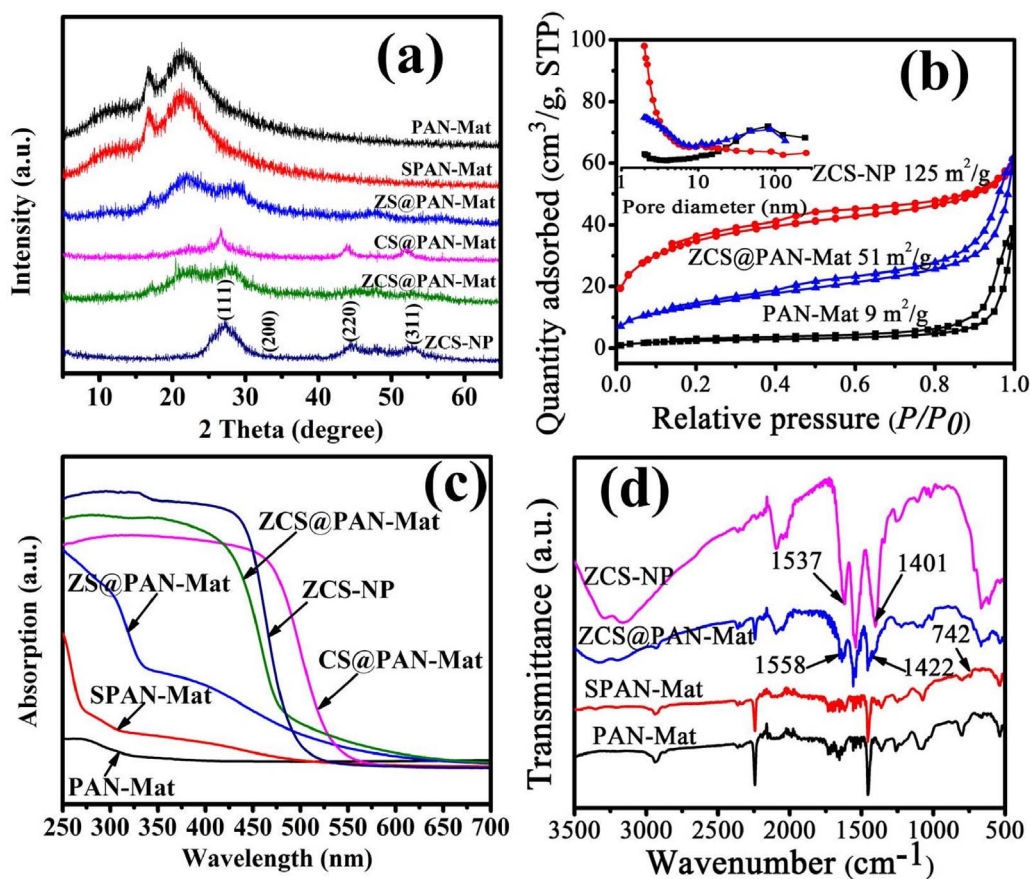**Fig. 3.** (a and b) FESEM images of PAN-Mat, (c) high-resolution TEM image of ZCS@PAN-Mat.

Fig. 4. (a) XRD patterns of the as-prepared samples, (b) N$_2$ adsorption-desorption isotherms and pore size distributions (inset) of PAN-Mat, ZCS-NP, and ZCS@PAN-Mat, (c) UV–vis diffuse reflection spectra of the as-prepared samples, (d) FT-IR spectra of PAN-Mat, SPAN-Mat, ZCS@PAN-Mat and ZCS-NP.

NP and ZCS@PAN-Mat are similar. It is understandable that these ratios are similar because the same weight ratios of reactants were used for the preparation of ZCS-NP and ZCS@PAN-Mat. Tracing back to the XRD results, the same crystal structures also indicate similar Zn/Cd ratios in

ZCS-NP and ZCS@PAN-Mat.

In order to measure the actual Zn/Cd ratio in Zn$_x$Cd$_{1-x}$S solid solution and get the real concentration of Zn$_x$Cd$_{1-x}$S in ZCS@PAN-Mat, inductively coupled plasma atomic emission spectrometry (ICP-AES)

Table 1
ICP-AES results obtained for ZCS-NP and ZCS@PAN-Mat.

Samples	ICP-AES (wt%)		Zn:Cd (mol%)
	Zn	Cd	
ZCS-NP	21.60	40.10	1:1.08 $Zn_{0.48}Cd_{0.52}S$
ZCS@PAN-Mat	13.12	20.30	1:0.90 $Zn_{0.53}Cd_{0.47}S$

analysis was performed for ZCS-NP and ZCS@PAN-Mat. The actual compositions of $Zn_xCd_{1-x}S$ solid solution in ZCS-NP and ZCS@PAN-Mat were calculated to be $Zn_{0.46}Cd_{0.54}S$ and $Zn_{0.53}Cd_{0.47}S$, respectively (Table 1). A little richer content of Zn in ZCS@PAN-Mat coincides with the slightly blue-shift of absorption edge in the UV–vis spectrum as compared with that of ZCS-NP. Overall, the molar Zn/Cd ratios are close to 1:1, excluding the $Zn_xCd_{1-x}S$ component effect on the photocatalytic performance of ZCS-NP and ZCS@PAN-Mat. Moreover, according to the ICP-AES results, the weight ratio of $Zn_{0.5}Cd_{0.5}S$ in ZCS@PAN-Mat can be calculated to be 45.39%.

XPS was used to investigate the surface chemical compositions and the chemical states of elements in the samples studied. Zn 2p, Cd 3d, S 2p, C 1s, N 1s and O 1s peaks were detected on the XPS survey scan of ZCS@PAN-Mat. Fig. 5 presents the high-resolution XPS spectra of C 1s, S 2p, Cd 3d and N 1s. As shown in Fig. 5a, the C 1s spectra of ZCS-NP, ZCS@PAN-Mat and PAN-Mat can be deconvoluted into three peaks. The peaks at 284.8 eV are assigned to C−C, C=C, and C−H bonds, which are caused by adventitious carbon [37,50]. The peak at 286.0 eV is related to the C≡N bonds and the peak at 288.8 eV (or 288.4 eV) is attributed to carboxyl carbon (O−C=O) [40]. The C≡N and O−C=O bonds in PAN-Mat are from PAN and intermediate of solvent (*N, N′*-

dimethylformamide), respectively. While, the O−C=O bonds and less C≡N bonds in ZCS-NP are caused by the intermediate of organic precursor (thiourea) and solvent (ethanol and *N, N′*-dimethylformamide). The O−C=O bonds from the intermediate and C≡N from PAN can be also observed in ZCS@PAN-Mat. In Fig. 5b, the S 2p spectra of ZCS-NP and ZCS@PAN-Mat (no S element signal can be detected in PAN-Mat) show obvious difference. The S 2p XPS spectrum of ZCS@PAN-Mat can be deconvoluted into four peaks at 162.8, 161.6, 168.3 and 169.5 eV. The former two peaks (the same binding energy with that in ZCS-NP) can be assigned to the S in $Zn_{0.5}Cd_{0.5}S$, the other two small peaks at 168.3 and 169.5 eV are attributed to the sulfone group (–SO_2–), which is due to the partial sulfurization of PAN during solvothermal process [51]. The S 2p XPS spectrum of SPAN-Mat (Fig. 6a) also shows clear peaks at 167.5 and 168.7 eV, which can be ascribed to the sulfone group (–SO_2–), and other two peaks located at 162.6 and 163.8 eV can be assigned to mercaptan group (–SH) [52]. These results provide direct evidence of PAN sulfurization during solvothermal process. Moreover, the shift in binding energies of sulfone group (–SO_2–) in ZCS@PAN-Mat indicates an intimate contact between surface deposits and sulfurized PAN substrate through the surface sulfone group (–SO_2–). The sulfurized PAN has more surface functional groups [53], which are beneficial for the uniform dispersion of surface deposits. Moreover, more surface S species in PAN nanofibers results in its better affinity to surface $Zn_xCd_{1-x}S$ deposits, accounting for the intimate contact between ZCS and PAN. Fig. 5c shows a comparison of Cd 3d spectra of ZCS-NP and ZCS@PAN-Mat. It should be noted that the Cd 3d binding energies of ZCS@PAN-Mat exhibit a positive shift as compared with that of ZCS-NP (pristine $Zn_{0.5}Cd_{0.5}S$). While, in Fig. 5d, the peak located at 404.8 eV can be caused by nitrates coming from reaction intermediate [52]. The binding energies at 399.0 eV (PAN-Mat) and 398.5 eV (ZCS@PAN-Mat) are related to C≡N bonds in PAN. The N 1s binding energy of ZCS@PAN-Mat (C≡N) exhibits a negative shift as compared with that of PAN-Mat
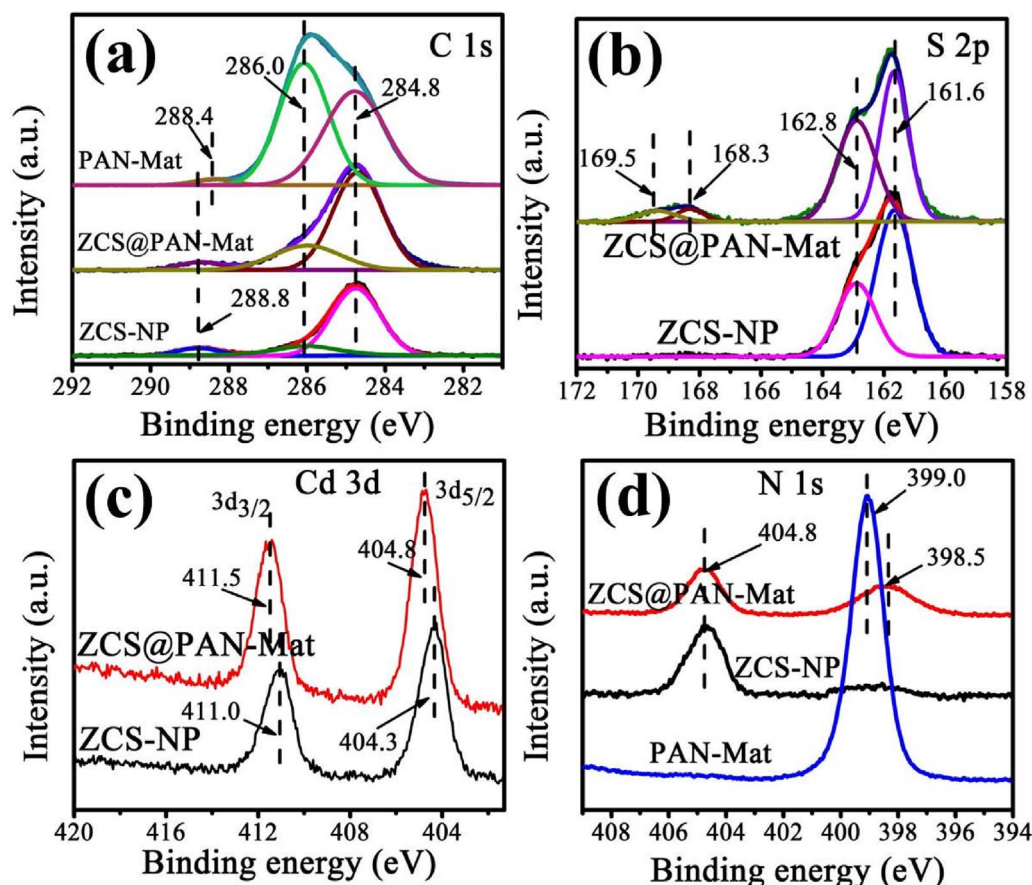

Fig. 5. (a) C 1s, (b) S 2p, (c) Cd 3d and (d) N 1s orbital XPS spectra of ZCS-NP, ZCS@PAN-Mat and PAN-Mat.
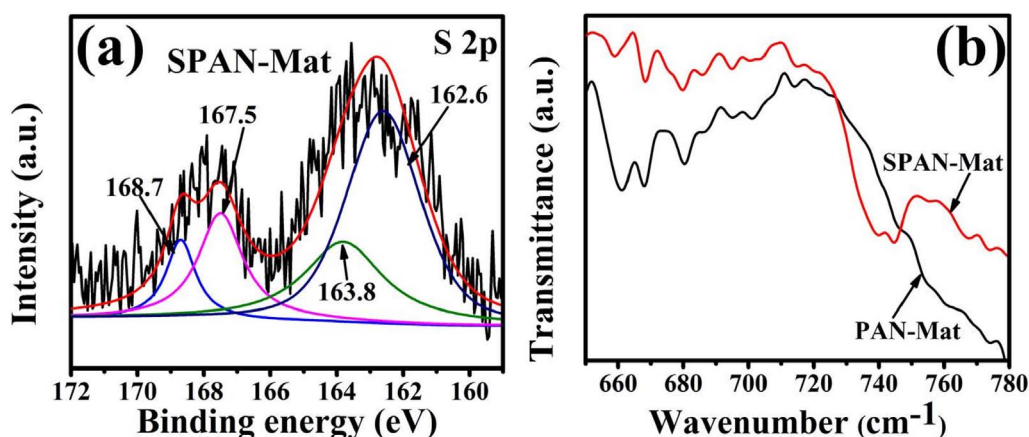
Fig. 6. (a) S 2p orbital XPS spectrum of SPAN-Mat, (b) FT-IR spectra of PAN-Mat and SPAN-Mat in the range of 650–780 cm^{-1}.
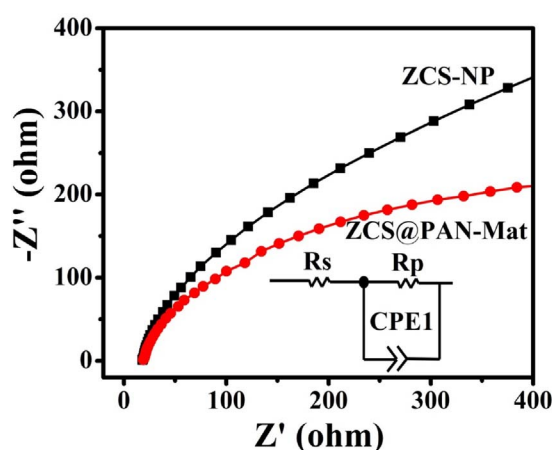

Fig. 7. Nyquist plots obtained of ZCS-NP and ZCS@PAN-Mat.
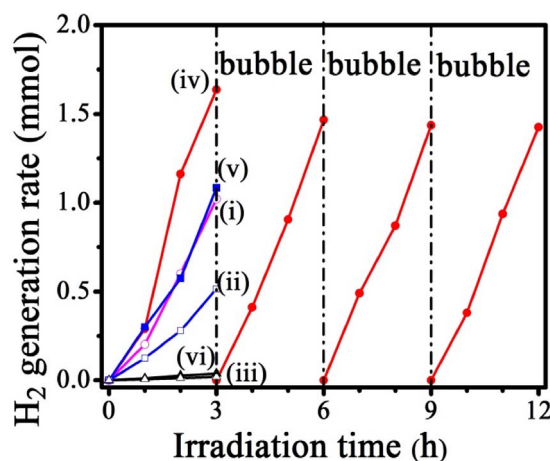

Fig. 9. Photocatalytic hydrogen generation under visible light. Comparison of photocatalytic H$_2$ evolution rate of ZCS-NP (i), CS-NP (ii), ZS-NP (iii), ZCS@PAN-Mat (iv), CS@PAN-Mat (v) ZS@PAN-Mat (vi) and under visible light irradiation ($\lambda > 420$ nm).

(pristine PAN). Since the electronegativities of Zn, Cd, S, and N are 1.65, 1.69, 2.58 and 3.04, respectively, the greater electronegativity of N can explain the binding energy negative shift of N and positive shift of Cd. The increased and decreased binding energies of Cd 3d and N 1s in ZCS@PAN-Mat further indicate a strong electronic coupling between Zn$_{0.5}$Cd$_{0.5}$S shell and PAN core.

An intimate contact and strong interaction between Zn$_{0.5}$Cd$_{0.5}$S and PAN greatly affects the durability and efficiency of ZCS@PAN-Mat. The strong interaction between Zn$_{0.5}$Cd$_{0.5}$S and PAN is also confirmed by Fourier transform infrared (FT-IR) spectra (Fig. 5d), in which the characteristic stretching modes of Zn-S bond in ZCS@PAN-Mat show slight shift as compared with that of ZCS-NP (for example, 1537 →

1558 cm^{-1} and 1401 → 1422 cm^{-1}), suggesting the strong interaction between Zn$_{0.5}$Cd$_{0.5}$S and PAN. Moreover, a small new band at about 742 cm^{-1} appears on the spectrum of SPAM-Mat (Fig. 6b), which can be attributed to C–S stretching modes, further implying the presence of sulfurized PAN.

3.3. Interfacial photoinduced charge transfer properties

The electrochemical impedance spectroscopy (EIS) was used to study the photoinduced interfacial charge transfer rate. As shown in
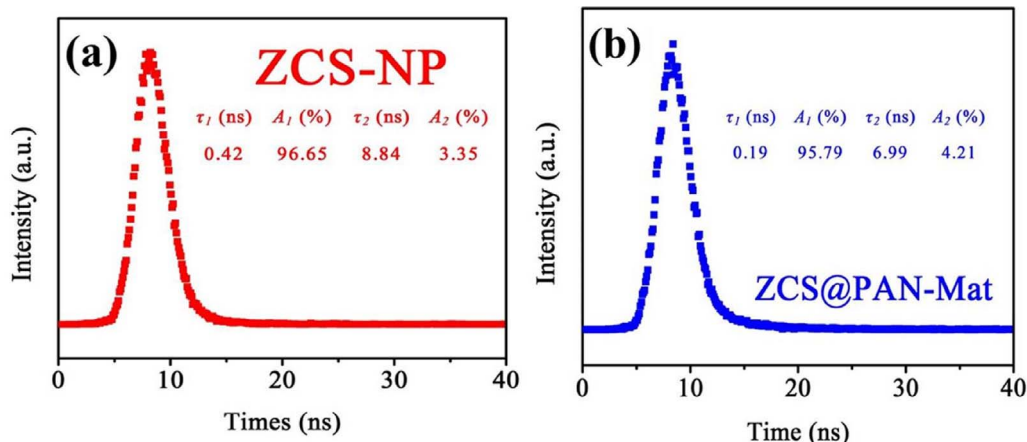
Fig. 8. Time-resolved transient PL decays of (a) ZCS-NP and (b) ZCS@PAN-Mat.
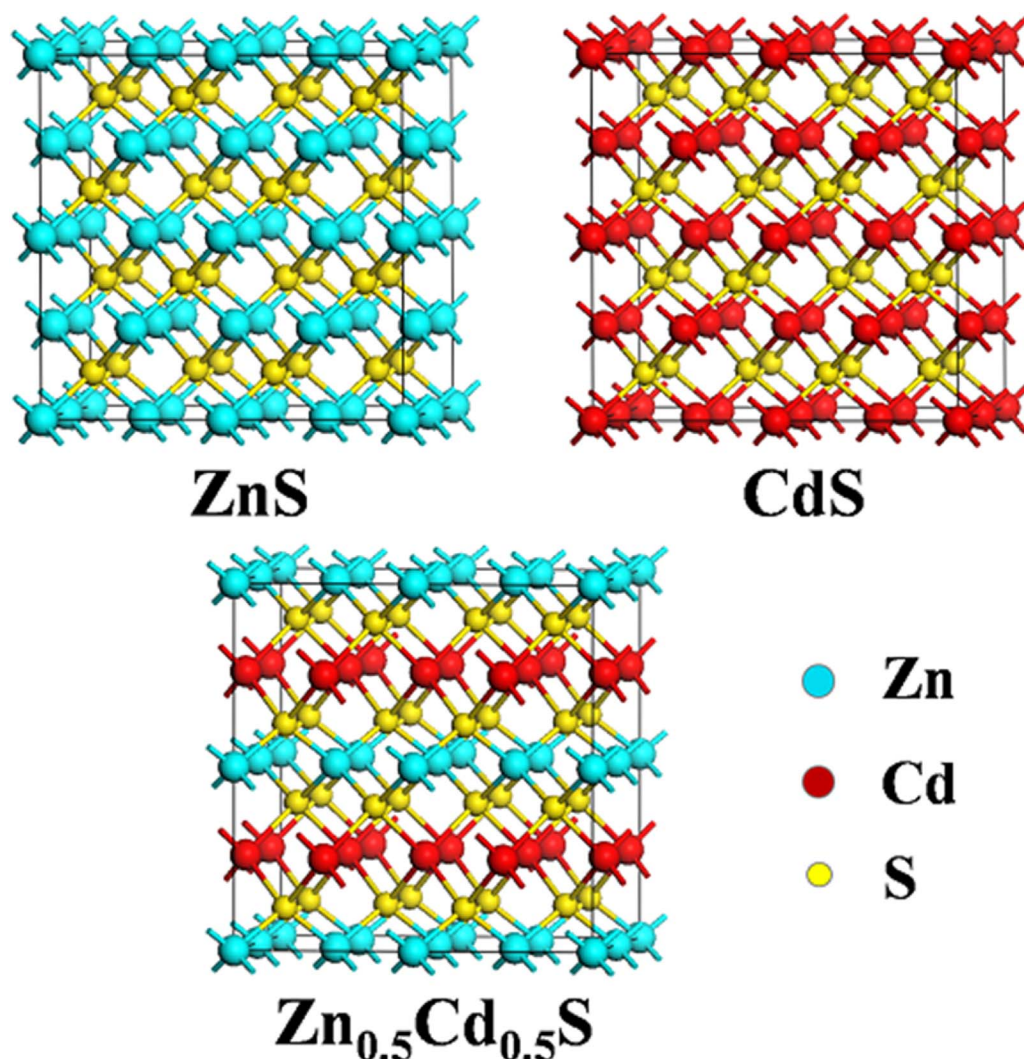
Fig. 10. Models for simulating the unit cells of ZnS (32 Zn atoms and 32 S atoms), CdS (32 Cd atoms and 32 S atoms), and $Zn_{0.5}Cd_{0.5}S$ (16 Zn atoms, 16 Cd atoms and 32 S atoms).

Fig. 7, the semicircular Nyquist plots of ZCS@PAN-Mat show an obviously decreased diameter than that of ZCS-NP. This means that the interfacial electron-transfer resistance in ZCS@PAN-Mat is smaller than that in ZCS-NP [54,55]. Herein, the smaller interfacial electron-transfer resistance of ZCS@PAN-Mat is due to the good dispersion of ZCS NPs and their ordered structure along PAN nanofibers. Contrarily, a serious aggregation of NPs in ZCS-NP sample and their disorderd structure increases the length of charge transfer path, resulting in larger interfacial electron-transfer resistance.

To provide further evidence on the charge migration and separation, the time-resolved transient photoluminescence (PL) spectroscopy was measured (Fig. 8). The lifetimes of PL were determined by a double-exponential fitting. As compared with the sample ZCS-NP, both the shorter lifetime and longer lifetime of ZCS@PAN-Mat decrease (from 0.42 ns to 0.19 ns and 8.84 ns to 6.99 ns). However, the percentage of shorter lifetime and longer lifetime almost has no change, indicating the same emission pathways in ZCS-NP and ZCS@PAN-Mat. The shorter lifetime is due to the decay from free exciton states. The longer lifetime is from the bound exciton states [56,57]. The decreased lifetimes indicate more nonradiative transitions existing in ZCS@PAN-Mat, which is induced by the easier exciton transfer from bulk to surface due to the shorter pathway caused by uniform dispersion of ZCS NPs. The aggregation of NPs in ZCS-NP increases the recombination probability of exciton, accounting for longer lifetime than that in ZCS@PAN-Mat. Moreover, as mentioned above, the one-dimensional (1D) core–shell $Zn_{0.5}Cd_{0.5}S$@PAN nanostructures have distinctive properties for rapid

diffusion-free electron transport along the axial direction [40,41,58]. These are key factors for the shorter emission lifetime and smaller interfacial electron-transfer resistance, which are beneficial for improving photocatalytic activity [59,60].

3.4. Photocatalytic hydrogen generation under visible light

The photocatalytic H_2-generation activities over ZCS-NP and ZCS@PAN-Mat were evaluated and shown in Fig. 9. The activities of control samples, CS-NP, CS@PAN-Mat, ZC-NP and ZS@PAN-Mat, are also provided. The amounts of photocatalysts in all systems studied were set as 50 mg. No photocatalytic activity was observed in the pure PAN-Mat due to its non-light-response. The ZCS-NP sample (pure $Zn_{0.5}Cd_{0.5}S$ NPs) displays a H_2 generation rate of 340 µmol h^{-1}. In contrast, the ZCS@PAN-Mat exhibits a H_2 generation rate of 475 µmol h^{-1}, which is higher than that of pure $Zn_{0.5}Cd_{0.5}S$ NPs. Moreover, the weight ratio of $Zn_{0.5}Cd_{0.5}S$ in ZCS@PAN-Mat was 45.39%. The actual activity of $Zn_{0.5}Cd_{0.5}S$ in ZCS@PAN-Mat should be much higher than that in ZCS-NP. Also, the apparent quantum efficiency of ZCS@PAN-Mat was calculated to be 27.4% at 420 nm. Moreover, the CS@PAN-Mat shows higher H_2 generation rate (361 µmol h^{-1}) than that of CS-NP (172 µmol h^{-1}). This difference further indicates that the sulfurized PAN substrate can enhance the activity of surface deposited photocatalyst. Both ZS@PAN-Mat and ZS-NP show negligible visible-light activity due to the wide band gap of ZnS (3.2 eV).

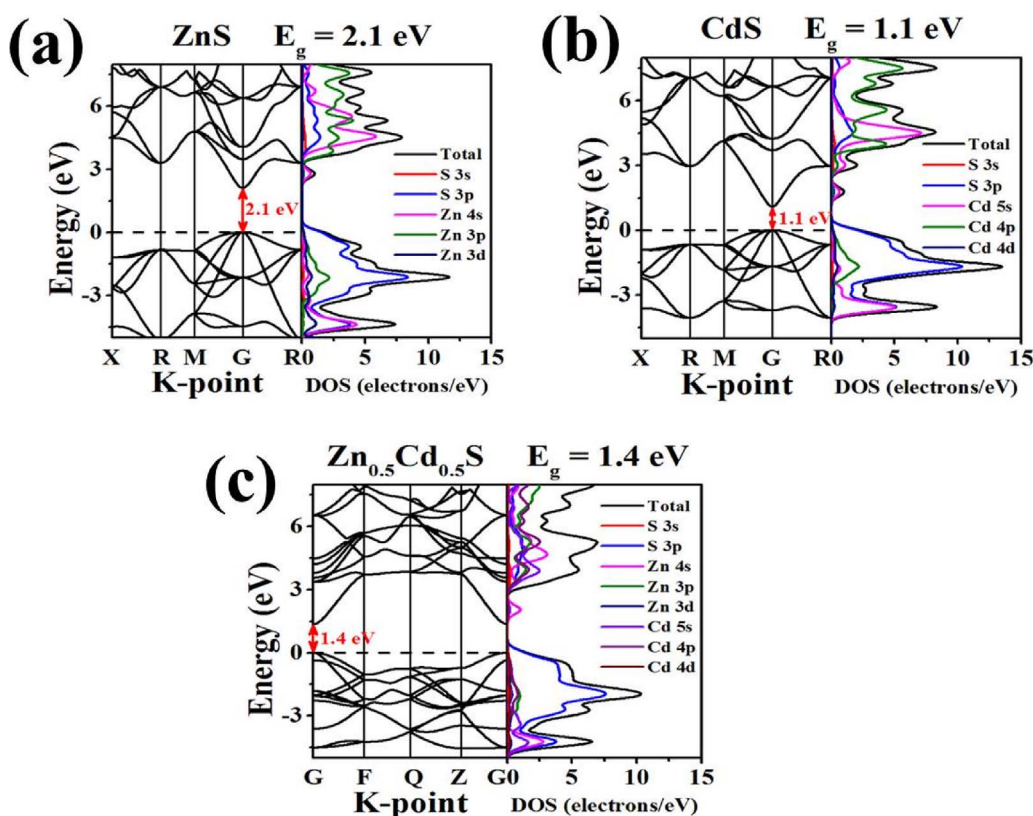A movie showing photocatalytic H_2-production over ZCS@PAN-Mat

Fig. 11. Calculated band structures and DOS of the simulated ZnS (a), CdS (b) and $Zn_{0.5}Cd_{0.5}S$ (c) models.

(Movie S1 in the Supporting Information) clearly exhibits hydrogen generation. As can be seen on this movie, H_2 gas is bubbling from the surface of ZCS@PAN-Mat during irradiation, and the shape of ZCS@PAN-Mat is preserved during the entire H_2-production process. Moreover, the photocatalytic stability of ZCS@PAN-Mat was examined by cycle stability tests. At the second cycle, the activity showed a slight decrease. No distinct decrease in the H_2 generation rate was observed in the next cycles (Fig. 9). It can be concluded that the ZCS@PAN-Mat is stable during photocatalytic reaction. Especially, after the cycle stability tests, ZCS@PAN-Mat can be easily taken out from the reaction solution by using tweezers, and the integrated shape of the mat is preserved. These results demonstrate that the ZCS@PAN-Mat can serve as a highly efficient and easily re-used photocatalyst for promising practical applications.

To further understand better photocatalytic activity of ZCS@PAN-Mat in comparison to the activities of CS@PAN-Mat and ZS@PAN-Mat, the band structure and adsorption properties of $Zn_{0.5}Cd_{0.5}S$, CdS and ZnS toward H_2O and H_2 molecules were investigated by density function theory (DFT) calculations. At first, three models were built to simulate the unit cells of $Zn_{0.5}Cd_{0.5}S$, ZnS and CdS (Fig. 10). The calculated band structures presented in Fig. 11 show that the band gaps of $Zn_{0.5}Cd_{0.5}S$, ZnS and CdS are 1.4, 2.1 and 1.1 eV, respectively. Although these values are smaller than the experimental values due to the well-known limitation of DFT calculations, $Zn_{0.5}Cd_{0.5}S$ has a middle band gap as compared with ZnS and CdS. It is noteworthy that the band gap of ZCS@PAN-Mat revealed by the UV–vis DRS spectrum is also between the values of both ZS@PAN-Mat and CS@PAN-Mat. In addition, the density of states (DOS) indicates that the valance band of these sulfides mainly consists of the S 3p orbital, and the conduction band is primarily composed of the outermost s and p orbitals of the metal atoms.

During the photocatalytic water splitting, good adsorption of H_2O and desorption of H_2 on the sample surface are extremely important. On the one hand, H_2O molecules split to produce H_2 only when they are first adsorbed on the photocatalyst. On the other hand, the generated H_2 molecules covering the sample surface will occupy part of the active sites for the photocatalytic reaction. The subsequent adsorption of H_2O can take place only when H_2 molecules detach from the sample and the fresh surface is re-exposed to the solution. Herein, the active sites of hydrogen generation are located on the surface of $Zn_{0.5}Cd_{0.5}S$. Various adsorption models were established by placing a single H_2O or H_2 molecule on the (111) facets of $Zn_{0.5}Cd_{0.5}S$, ZnS and CdS, which are mainly exposed facets as indicated by XRD analysis. Thus, H_2O molecules are mainly adsorbed on these (111) facets. The models after geometry optimizations are illustrated in Fig. 12. The adsorption energy (E_{ads}) of H_2O was defined as:

$$E_{ads}(H_2O) = E(H_2O/MS) - E(MS) - E(H_2O)$$

where MS represents $Zn_{0.5}Cd_{0.5}S$ (111), ZnS (111) or CdS (111), $E(H_2O)$ is the energy of a single H_2O molecule, $E(H_2O/MS)$ and $E(MS)$ are the total energy of MS system with and without H_2O, respectively. Similarly, the adsorption energy of H_2 was defined as:

$$E_{ads}(H_2) = E(H_2/MS) - E(MS) - E(H_2)$$

where $E(H_2)$ is the energy of a single H_2 molecule, $E(H_2/MS)$ and $E(MS)$ are the total energy of MS system with and without H_2, respectively. According to these definitions, a negative value of the E_{ads} indicates that the adsorption is exothermic and thermodynamically stable, and a positive value indicates that the adsorption is endothermic and thermodynamically unstable. The calculated adsorption energies of H_2O and H_2 based on these models are listed in Table 2. As can be seen, the adsorption energies of H_2O on the (111) facets of $Zn_{0.5}Cd_{0.5}S$, ZnS and CdS are -0.6, -1.0, and -0.5 eV, respectively, indicating that the adsorption performance of H_2O is in the following order: ZnS (111) > $Zn_{0.5}Cd_{0.5}S$ (111) > CdS (111). Meanwhile, the adsorption energies of H_2 on the (111) facets of $Zn_{0.5}Cd_{0.5}S$, ZnS and CdS are 0.0031, -0.0003, and 0.0009 eV, respectively. A negative value of adsorption energy indicates that adsorption is exothermic and thermodynamically stable, and a positive value indicates that adsorption is endothermic and thermodynamically unstable. These results suggest
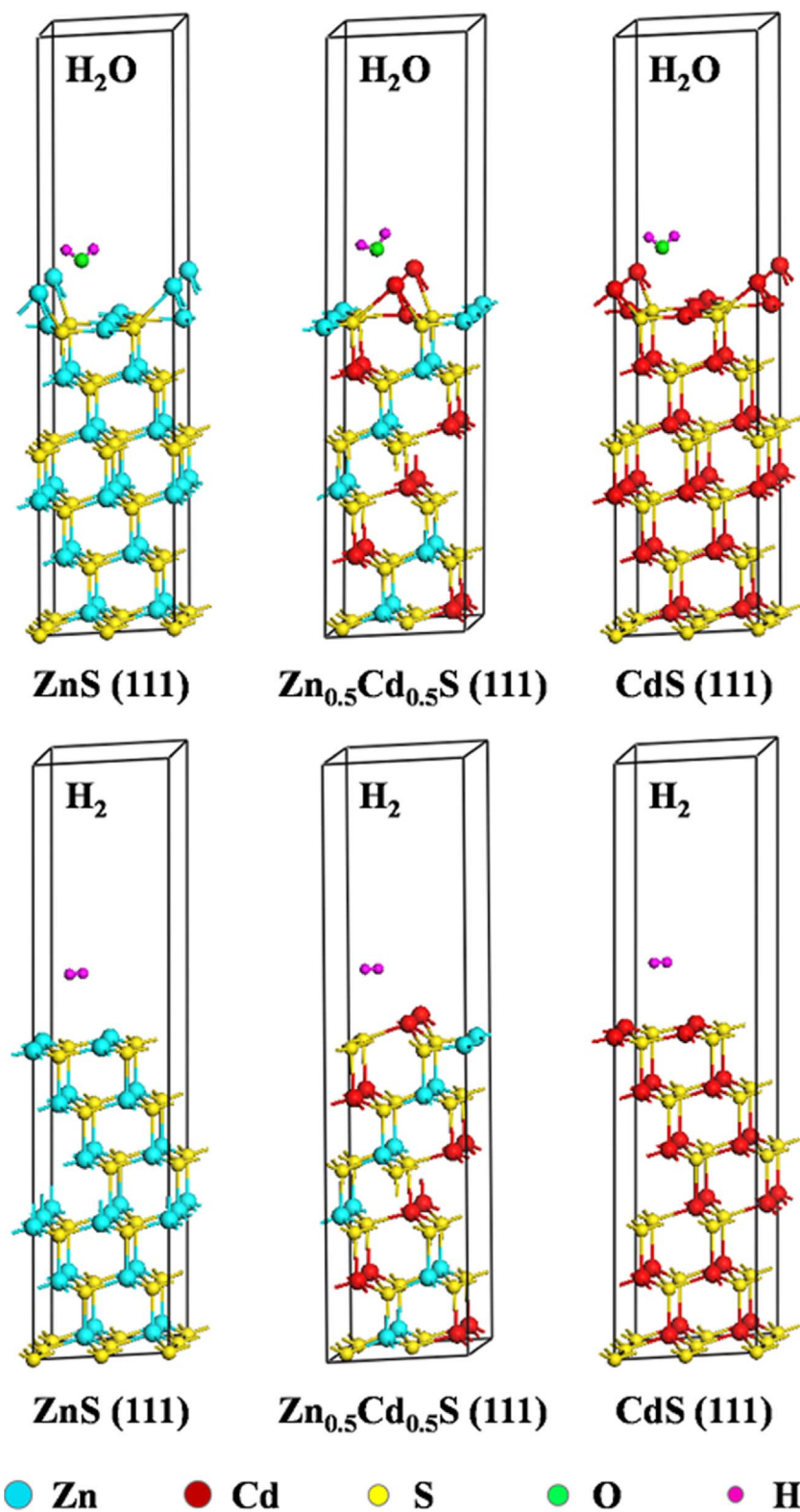
Fig. 12. The optimized configurations of a single H_2O or H_2 molecule adsorbed on the (111) facets of $Zn_{0.5}Cd_{0.5}S$, ZnS and CdS based on the DFT calculations. Each model contains 24 S atoms and 24 metal (Zn, Cd) atoms, as well as a H_2O or H_2 molecule. A vacuum space of 15 Å was used to avoid interactions between periodic slabs.

that the generated H_2 in the photocatalytic reaction does not tend to be adsorbed on the surface of $Zn_{0.5}Cd_{0.5}S$. In other words, the generated H_2 on the surface of $Zn_{0.5}Cd_{0.5}S$ photocatalyst is quickly desorbed from the surface and the active sites are not covered by the generated H_2. The above comparison shows that $Zn_{0.5}Cd_{0.5}S$ has smaller band gap than ZnS, stronger adsorption ability toward H_2O than that of CdS and highest desorption capability toward H_2. These advantages of $Zn_{0.5}Cd_{0.5}S$ greatly contribute to the superior photocatalytic H_2-production activity of $Zn_{0.5}Cd_{0.5}S$ as compared to ZnS and CdS alone.

For better illustrating the advantages of ZCS@PAN-Mat composite photocatalyst, Fig. 13 shows a schematic comparison of the structures of ZCS-NP and ZCS@PAN-Mat. During solvothermal preparation of ZCS-NP, numerous small crystal nuclei are first produced by homogeneous nucleation, and then grow and aggregate to form large secondary particles. The FESEM images of ZCS-NP in Fig. 14 show clearly the aggregation phenomenon of ZCS NPs, which reduces the surface

Table 2
Calculated band gaps of photocatalysts and adsorption energies of H_2O and H_2 on (111) facet.

Samples	Band gap (eV)	Adsorption energy (eV) of H_2O	Adsorption energy (eV) of H_2
$Zn_{0.5}Cd_{0.5}S$	1.4	−0.6	0.0031
ZnS	2.1	−1.0	−0.0003
CdS	1.1	−0.5	0.0009

Fig. 13. Comparison of the main structure features of ZCS-NP (a), ZCS@PAN-Mat (b) and leaf (c) (the red arrows in ZCS@PAN-Mat represent the light). (For interpretation of the references to colour in this figure legend, the reader is referred to the web version of this article.)

active sites and utilization of light in photocatalytic reactions. Moreover, under light irradiation, NPs with high surface energy also tend to further aggregate, which is extremely unfavorable for photocatalytic reactions. A serious agglomeration of NPs not only greatly reduces the rate of redox reactions due to the quick recombination of photo-generated electron–hole pairs, but also increases the diffusion barriers of reactants and products, which are both unfavorable for the photocatalytic reactions [61]. Contrarily, the aggregation of NPs can be completely inhibited in the case of ZCS@PAN-Mat because ZCS NPs are firmly attached on the surface of PAN nanofibers. Based on the above results and porosity analysis (Fig. 4b), the leaf-like morphology of ZCS@PAN-Mat can enhance diffusion kinetics of reactants and products due to its macroscopically flat and internally hierarchical porous structure, which is beneficial for reducing mass-transport barriers and improving the photocatalytic efficiency. Also, the leaf-like hierarchically porous structure is conducive to capture light through multiple reflections and scattering within hierarchical pore channels in the mat as compared with the agglomerated ZCS NPs (Fig. 13a) [61–63].

The structure of ZCS@PAN-Mat is further compared with that of natural leaf and shown in Fig. 13b and Fig. 13c. Firstly, both leaf and ZCS@PAN-Mat have flat and flexible shapes (Figs. 1 and 2). This feature

of leaf has been proved to be especially efficient to utilize light and capture of reactants (CO_2 and H_2O) due to its large flat surface. The flat and flexible shape of ZCS@PAN-Mat functions similarly as leaf in enhancing photocatalytic H_2-generation activity. Secondly, the presence of stomata on the surface of leaf acts as network of channels facilitating the transport of gaseous reactants and products. Likewise, in the case of ZCS@PAN-Mat, the presence of hierarchically porous structure can not only enhance diffusion kinetics of reactants and products by reducing mass-transport barriers, but also increase capture of light by creating longer light traveling paths through multiple reflections and scattering [61,62]. Thirdly, the uniformly dispersed ZCS NPs on PAN mat play a similar role as chlorophylls immobilized on the flexible leaf skeleton in photosynthesis, which are better exposed to light and H_2O molecules. Thus, it is not surprising that the flexible ZCS@PAN-Mat photocatalyst with bio-inspired leaf structure shows higher photocatalytic hydrogen generation activity than ZCS NPs. Moreover, the flexible feature of ZCS@PAN-Mat photocatalyst has a great potential for extending the range of application conditions beyond those used for powder photo-catalysts, such as wearable photocatalyst devices.

4. Conclusion

In summary, a leaf-like flexible bio-inspired ZCS@PAN-Mat photo-catalyst with high H_2-production performance was developed and explored. This photocatalyst showed a H_2-production rate of 475 µmol h^{-1} per 50 mg of ZCS@PAN-Mat and an apparent QE of 27.4% at 420 nm, which are higher than those obtained for pure $Zn_{0.5}Cd_{0.5}S$ NPs. This enhancement in the photocatalytic H_2-production performance of $Zn_{0.5}Cd_{0.5}S$@PAN-Mat can be attributed to its flat and hierarchically porous structure, which can greatly enhance the diffusion/transfer kinetics of reactants and products, and increase the utilization of light through the multiple reflections and scattering of light inside hierarchical pore channels. Another obvious advantage of the ZCS@PAN-Mat photocatalyst is its flexibility and recyclability, which endow its high stability in photocatalytic reactions. This flexible leaf-like bio-inspired photocatalyst is very promising due to its potential for a wide spectrum of applications ranging from catalysis, photocatalysis, separation to solar cells and purification processes.
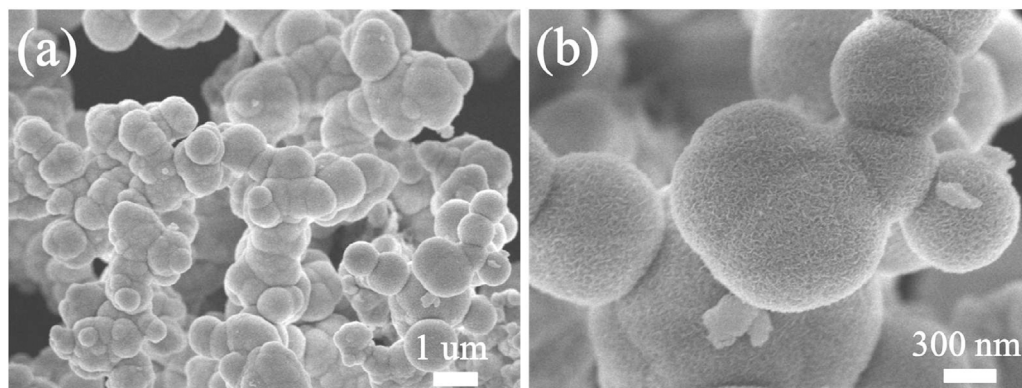
Fig. 14. The FESEM images (a and b) of ZCS-NP.

Appendix A. Supplementary data

Supplementary data associated with this article can be found, in the online version, at http://dx.doi.org/10.1016/j.apcatb.2017.08.034.

References

[1] A. Fujishima, K. Honda, Electrochemical photolysis of water at a semiconductor electrode, Nature 238 (1972) 37–38.

[2] M.G. Walter, E.L. Warren, J.R. McKone, S.W. Boettcher, Q. Mi, E.A. Santori, N.S. Lewis, Solar water splitting cells, Chem. Rev. 110 (2010) 6446–6473.

[3] Y. Hou, B.L. Abrams, P.C.K. Vesborg, M.E. Bjorketun, K. Herbst, L. Bech, A.M. Setti, C.D. Damsgaard, T. Pedersen, O. Hansen, J. Rossmeisl, S. Dahl, J.K. Norskov, I. Chorkendorff, Bioinspired molecular co-catalysts bonded to a silicon photocathode for solar hydrogen evolution, Nat. Mater. 10 (2011) 434–438.

[4] N.S. Lewis, Toward cost-effective solar energy use, Science 315 (2007) 798–801.

[5] S. Hong, D.P. Kumar, D.A. Reddy, J. Choi, T.K. Kim, Excellent photocatalytic hydrogen production over CdS nanorods via using noble metal-free copper molybdenum sulfide (Cu_2MoS_4) nanosheets as co-catalysts, Appl. Surf. Sci. 396 (2017) 421–429.

[6] D. Ni, H. Shen, H. Li, Y. Ma, T. Zhai, Synthesis of high efficient Cu/TiO_2 photocatalysts by grinding and their size-dependent photocatalytic hydrogen production, Appl. Surf. Sci. 409 (2017) 241–249.

[7] Q. Xu, B. Cheng, J. Yu, G. Liu, Making co-condensed amorphous carbon/g-C_3N_4 composites with improved visible-light photocatalytic H_2-production performance using Pt as cocatalyst, Carbon 118 (2017) 241–249.

[8] S. Cao, J. Yu, Carbon-based H_2-production photocatalytic materials, J. Photochem. Photobiol. C 27 (2016) 72–99.

[9] C. Liu, B.C. Colon, M. Ziesack, P.A. Silver, D.G. Nocera, Water splitting-biosynthetic system with CO_2 reduction efficiencies exceeding photosynthesis, Science 352 (2016) 1210–1213.

[10] Y. Dong, L. Kong, G. Wang, P. Jiang, N. Zhao, H. Zhang, Photochemical synthesis of Co_xP as cocatalyst for boosting photocatalytic H_2 production via spatial charge separation, Appl. Catal. B 211 (2017) 245–251.

[11] D.P. Kumar, S. Hong, D.A. Reddy, T.K. Kim, Ultrathin MoS_2 layers anchored exfoliated reduced graphene oxide nanosheet hybrid as a highly efficient cocatalyst for CdS nanorods towards enhanced photocatalytic hydrogen production, Appl. Catal. B 212 (2017) 7–14.

[12] D. Dai, H. Xu, L. Ge, C. Han, Y. Gao, S. Li, Y. Lu, In-situ synthesis of CoP co-catalyst decorated $Zn_{0.5}Cd_{0.5}S$ photocatalysts with enhanced photocatalytic hydrogen production activity under visible light irradiation, Appl. Catal. B 217 (2017) 429–436.

[13] B. Wang, J. Zhang, F. Huang, Enhanced visible light photocatalytic H_2 evolution of metal-free g-C_3N_4/SiC heterostructured photocatalysts, Appl. Surf. Sci. 391 (2017) 449–456.

[14] F. Cheng, H. Yin, Q. Xiang, Low-temperature solid-state preparation of ternary CdS/g-C_3N_4/CuS nanocomposites for enhanced visible-light photocatalytic H_2-production activity, Appl. Surf. Sci. 391 (2017) 432–439.

[15] H. Gao, P. Zhang, J. Hu, J. Pan, J. Fan, G. Shao, One-dimensional Z-scheme TiO_2/WO_3/Pt heterostructures for enhanced hydrogen generation, Appl. Surf. Sci. 391 (2017) 211–217.

[16] J. Zhang, J. Yu, M. Jaroniec, J.R. Gong, Noble metal-free reduced graphene oxide-$Zn_xCd_{1-x}S$ nanocomposite with enhanced solar photocatalytic H_2-production performance, Nano Lett. 12 (2012) 4584–4589.

[17] M.G. Kibria, F.A. Chowdhury, S. Zhao, B. AlOtaibi, M.L. Trudeau, H. Guo, Z. Mi, Visible light-driven efficient overall water splitting using p-type metal-nitride nanowire arrays, Nat. Commun. 6 (2015) 6797.

[18] Q. Li, B.D. Guo, J. Yu, J.R. Ran, B.H. Zhang, H.J. Yan, J.R. Gong, Highly efficient visible-light-driven photocatalytic hydrogen production of CdS-cluster-decorated graphene nanosheets, J. Am. Chem. Soc. 133 (2011) 10878–10884.

[19] L. Li, J. Yan, T. Wang, Z.-J. Zhao, J. Zhang, J. Gong, N. Guan, Sub-10 nm rutile titanium dioxide nanoparticles for efficient visible-light-driven photocatalytic hydrogen production, Nat. Comm. 6 (2015) 5881.

[20] Y.H. Ng, A. Iwase, A. Kudo, R. Amal, Reducing graphene oxide on a visible-light $BiVO_4$ photocatalyst for an enhanced photoelectrochemical water splitting, J. Phys. Chem. Lett. 1 (2010) 2607–2612.

[21] J.Y. Shi, H. Cui, Z.X. Liang, X.H. Lu, Y.X. Tong, C.Y. Su, H. Liu, The roles of defect states in photoelectric and photocatalytic processes for $Zn_xCd_{1-x}S$, Energy Environ. Sci. 4 (2011) 466–470.

[22] K. Li, R. Chen, S.L. Li, M. Han, S.L. Xie, J.C. Bao, Z.H. Dai, Y.Q. Lan, Self-assembly of a mesoporous ZnS/mediating interface/CdS heterostructure with enhanced visible-light hydrogen-production activity and excellent stability, Chem. Sci. 6 (2015) 5263–5268.

[23] Q. Li, X. Li, S. Wageh, A.A. Al-Ghamdi, J. Yu, CdS/graphene nanocomposite photocatalysts, Adv. Energy Mater. 5 (2015) 1500010.

[24] Q. Gu, H. Sun, Z. Xie, Z. Gao, C. Xue, MoS_2-coated microspheres of self-sensitized carbon nitride for efficient photocatalytic hydrogen generation under visible light irradiation, Appl. Surf. Sci. 396 (2017) 1808–1815.

[25] A. Meng, J. Zhang, D. Xu, B. Cheng, J. Yu, Enhanced photocatalytic H_2-production activity of anatase TiO_2 nanosheet by selectively depositing dual-cocatalysts on {101} and {001} facets, Appl. Catal. B 198 (2016) 286–294.

[26] R. Zhang, X. Wang, J. Song, Y. Si, X. Zhuang, J. Yu, B. Ding, In situ synthesis of flexible hierarchical TiO_2 nanofibrous membranes with enhanced photocatalytic activity, J. Mater. Chem. A 3 (2015) 22136–22144.

[27] D. Wang, Y. Liu, C. Wang, F. Zhou, W. Liu, Highly flexible coaxial nanohybrids

[28] made from porous TiO_2 nanotubes, ACS Nano 3 (2009) 1249–1257.

[29] X.F. Wang, X.H. Lu, B. Liu, D. Chen, Y.X. Tong, G.Z. Shen, Flexible energy-storage devices: design consideration and recent progress, Adv. Mater. 26 (2014) 4763–4782.

[29] L. Li, Z. Wu, S. Yuan, X.B. Zhang, Advances and challenges for flexible energy storage and conversion devices and systems, Energy Environ. Sci. 7 (2014) 2101–2122.

[30] Y.K. Kim, M. Kim, S.-H. Hwang, S.K. Lim, H. Park, S. Kim, CdS-loaded flexible carbon nanofiber mats as a platform for solar hydrogen production, Int. J. Hydrogen Energy 40 (2015) 136–145.

[31] J. Manna, S. Goswami, N. Shilpa, N. Sahu, R.K. Rana, Biomimetic method to assemble nanostructured Ag@ZnO on cotton fabrics: application as self-cleaning flexible materials with visible-light photocatalysis and antibacterial activities, ACS Appl. Mater. Interfaces 7 (2015) 8076–8082.

[32] F. Kayaci, C. Ozgit-Akgun, I. Donmez, N. Biyikli, T. Uyar, Polymer-inorganic coreshell nanofibers by electrospinning and atomic layer deposition: flexible nylon-ZnO core-shell nanofiber mats and their photocatalytic activity, ACS Appl. Mater. Interfaces 4 (2012) 6185–6194.

[33] Y.J. Chen, G.H. Tian, Z.Y. Ren, K. Pan, Y.H. Shi, J.Q. Wang, H.G. Fu, Hierarchical core-shell carbon nanofiber@$ZnIn_2S_4$ composites for enhanced hydrogen evolution performance, ACS Appl. Mater. Interfaces 6 (2014) 13841–13849.

[34] Z. Han, Y. Dong, S. Dong, Copper-iron bimetal modified PAN fiber complexes as novel heterogeneous Fenton catalysts for degradation of organic dye under visible light irradiation, J. Hazard. Mater. 189 (2011) 241–248.

[35] F. He, G. Chen, Y. Yu, S. Hao, Y. Zhou, Y. Zheng, Facile approach to synthesize g-PAN/g-C_3N_4 composites with enhanced photocatalytic H_2 evolution activity, ACS Appl. Mater. Interfaces 6 (2014) 7171–7179.

[36] J.S. Im, M. Il Kim, Y.-S. Lee, Preparation of PAN-based electrospun nanofiber webs containing TiO_2 for photocatalytic degradation, Mater. Lett. 62 (2008) 3652–3655.

[37] Y. Chen, Z. Li, X. Lou, General formation of $M_xCo_{3-x}S_4$ (MNi, Mn Zn) hollow tubular structures for hybrid supercapacitors, Angew. Chem. Int. Ed. 54 (2015) 1–5.

[38] Q. Li, H. Meng, P. Zhou, Y. Zheng, J. Wang, J. Yu, J. Gong, $Zn_{1-x}Cd_xS$ solid solutions with controlled bandgap and enhanced visible-light photocatalytic H_2-production activity, ACS Catal. 3 (2013) 882–889.

[39] J. Zhang, L. Qi, J. Ran, J. Yu, S.Z. Qiao, Ternary NiS/$Zn_xCd_{1-x}S$/reduced graphene oxide nanocomposites for enhanced solar photocatalytic H_2-production activity, Adv. Energy Mater. 4 (2014) 1301925.

[40] J. Fu, S. Cao, J. Yu, J. Low, Y. Lei, Enhanced photocatalytic CO_2-reduction activity of electrospun mesoporous TiO_2 nanofibers by solvothermal treatment, Dalton Trans. 43 (2014) 9158–9165.

[41] S. Choi, S. Kim, S. Lim, H. Park, Photocatalytic comparison of TiO_2 nanoparticles and electrospun TiO_2 nanofibers: effectsof mesoporosity and interparticle charge transfer, J. Phys. Chem. C 114 (2010) 16475–16480.

[42] Q. Li, H. Meng, J. Yu, W. Xiao, Y. Zheng, J. Wang, Enhanced photocatalytic hydrogen-production performance of graphene-$Zn_xCd_{1-x}S$ composites by using an organic S source, Chem. Eur. J. 20 (2014) 1176–1185.

[43] C. Wang, L. Wang, J. Jin, J. Liu, Y. Li, M. Wu, L. Chen, B. Wang, X. Yang, B.-L. Su, Probing effective photocorrosion inhibition and highly improved photocatalytic hydrogen production on monodisperse PANI@CdS core-shell nanospheres, Appl. Catal. B 188 (2016) 351–359.

[44] S. Ma, J. Xie, J. Wen, K. He, X. Li, W. Liu, X. Zhang, Constructing 2D layered hybrid CdS nanosheets/MoS_2 heterojunctions for enhanced visible-light photocatalytic H_2 generation, Appl. Surf. Sci. 391 (2017) 580–591.

[45] J. Zhang, S. Wageh, A. Al-Ghamdi, J. Yu, New understanding on the different photocatalytic activity of wurtzite and zinc-blende CdS, Appl. Catal. B 192 (2016) 101–107.

[46] R. Prasanth, V. Aravindan, M. Srinivasan, Novel polymer electrolyte based on cobweb electrospun multi component polymer blend of polyacrylonitrile/poly(methyl methacrylate)/polystyrene for lithium ion batteries—Preparation and electrochemical characterization, J. Power Sources 202 (2012) 299–307.

[47] K.S.W. Sing, D.H. Everett, R.A.W. Haul, L. Moscou, R.A. Pierotti, J. Rouquerol, T. Siemieniewska, Reporting physisorption data for gas/solid systems with special reference to the determination of surface area and porosity, Pure Appl. Chem. 54 (1982) 2201–2218.

[48] X. Cui, Y.F. Zheng, H.Y. Yin, X.C. Song, Novel C_3N_4/$Zn_{1-x}Cd_xS$ heterostructures with adjustment of the band gap and their visible light photocatalytic properties, Phys. Chem. Chem. Phys. 17 (2015) 29354–29362.

[49] S. Shen, Q. Wang, Rational tuning the optical properties of metal sulfide nanocrystals and their applications, Chem. Mater. 25 (2013) 1166–1178.

[50] Q. Liang, Z. Li, X. Yu, Z.-H. Huang, F. Kang, Q.-H. Yang, Macroscopic 3D porous graphitic carbon nitride monolith for enhanced photocatalytic hydrogen evolution, Adv. Mater. 27 (2015) 4634–4639.

[51] L. Wang, J. Zhao, X. He, C. Wan, Kinetic investigation of sulfurized polyacrylonitrile cathode material by electrochemical impedance spectroscopy, Electrochim. Acta 56 (2011) 5252–5256.

[52] J.F. Moulder, W.F. Strickle, P.E. Sobol, K.D. Bomben, Handbook of X-ray Photoelectron Spectroscopy, Perkin-Elmer Corporation, Minnesota, USA, 1992.

[53] B.R. Wu, Q. Liu, D.B. Mu, Y.H. Ren, Y. Li, L. Wang, H.L. Xu, F. Wu, New desolvated gel electrolyte for rechargeable lithium metal sulfurized polyacrylonitrile (S-PAN) battery, J. Phys. Chem. C 118 (2014) 28369–28376.

[54] P. Kuang, L. Zhang, B. Cheng, J. Yu, Enhanced charge transfer kinetics of Fe_2O_3/CdS composite nanorod arrays using cobalt-phosphate as cocatalyst, Appl. Catal. B 218 (2017) 570–580.

[55] Z. He, J. Fu, B. Cheng, J. Yu, S. Cao, $Cu_2(OH)_2CO_3$ clusters: novel noble-metal-free cocatalysts for efficient photocatalytic hydrogen production from water splitting, Appl. Catal. B 205 (2017) 104–111.

[56] Z. Zhang, J. Huang, M. Zhang, Q. Yuan, B. Dong, Ultrathin hexagonal SnS_2 nanosheets coupled with g-C_3N_4 nanosheets as 2D/2D heterojunction photocatalysts toward high photocatalytic activity, Appl. Catal. B 163 (2015) 298–305.

[57] J. Lim, B.G. Jeong, M. Park, J.K. Kim, J.M. Pietryga, Y.S. Park, V.I. Klimov, C. Lee, D.C. Lee, W.K. Bae, Influence of shell thickness on the performance of light-emitting devices based on $CdSe/Zn_{1-x}Cd_xS$ core/shell heterostructured quantum dots, Adv. Mater. 26 (2014) 8034–8040.

[58] R.S. Devan, R.A. Patil, J.-H. Lin, Y.-R. Ma, One-dimensional metal-oxide nanostructures: recent developments in synthesis, characterization, and applications, Adv. Funct. Mater. 22 (2012) 3326–3370.

[59] R. Marschall, Semiconductor composites: strategies for enhancing charge carrier separation to improve photocatalytic activity, Adv. Funct. Mater. 24 (2014)

[60] J. Low, J. Yu, M. Jaroniec, S. Wageh, A.A. Al-Ghamdi, Heterojunction photocatalysts, Adv. Mater. 29 (2017) 1601694.

[61] X. Li, J. Yu, M. Jaroniec, Hierarchical photocatalysts, Chem. Soc. Rev. 45 (2016) 2603–2636.

[62] Q. Xiang, B. Cheng, J. Yu, Hierarchical porous CdS nanosheet-assembled flowers with enhanced visible-light photocatalytic H_2-production performance, Appl. Catal. B 138 (2013) 299–303.

[63] J. Fu, B. Zhu, C. Jiang, B. Cheng, W. You, J. Yu, Hierarchical porous O-doped g-C_3N_4 with enhanced photocatalytic CO_2 reduction activity, Small 13 (2017) 1603938.

2421–2440.